



## RESEARCH ARTICLE

10.1029/2023JA031541

### Key Points:

- Machine learning was used to identify harmonics of Ionospheric Alfvén Resonances and harmonic frequency separation for 9 years of data
- The harmonic frequency separation was modeled for this data set and comparisons were made between model and data
- The model and data follow the same general trends, with higher frequencies corresponding to lower plasma mass density

### Correspondence to:

R. M. Hodnett,  
[rmh38@leicester.ac.uk](mailto:rmh38@leicester.ac.uk)

### Citation:

Hodnett, R. M., Yeoman, T. K., Beggan, C. D., & Wright, D. M. (2023). Climatology of the harmonic frequency separation of ionospheric Alfvén resonances at Eskdalemuir Observatory, UK. *Journal of Geophysical Research: Space Physics*, 128, e2023JA031541. <https://doi.org/10.1029/2023JA031541>

Received 30 MAR 2023  
Accepted 19 MAY 2023

©2023. The Authors.

This is an open access article under the terms of the [Creative Commons Attribution License](https://creativecommons.org/licenses/by/4.0/), which permits use, distribution and reproduction in any medium, provided the original work is properly cited.

# Climatology of the Harmonic Frequency Separation of Ionospheric Alfvén Resonances at Eskdalemuir Observatory, UK

R. M. Hodnett<sup>1</sup> , T. K. Yeoman<sup>1</sup> , C. D. Beggan<sup>2</sup> , and D. M. Wright<sup>1</sup>

<sup>1</sup>School of Physics and Astronomy, University of Leicester, Leicester, UK, <sup>2</sup>British Geological Survey, Edinburgh, UK

**Abstract** We extracted the harmonic frequency separation ( $\Delta f$ ) of Ionospheric Alfvén Resonances (IAR) observed in the Eskdalemuir induction coil magnetometer data for the 9 year data set of 2013–2021. To obtain  $\Delta f$  values, we used a machine learning technique that identifies the harmonics and from this we calculated the average separation. To investigate the climatology of the IAR, we have modeled the  $\Delta f$  of the IAR for the data set using a time of flight calculation with model Alfvén velocity profiles. When analyzing  $\Delta f$  from the model and data, we found that in general they follow the same trends. The modeled  $\Delta f$  and  $\Delta f$  from the data both show an inverse correlation with  $f_oF2$ , which confirms that the frequencies of the IAR are controlled by electron density. It follows that  $\Delta f$  is greater around midnight and during the winter months, due to the decrease in plasma mass density. Variability is also reflected when comparing yearly trends in  $\Delta f$  with the sunspot number; higher frequencies are observed and modeled at low sunspot number. It is difficult to examine trends with instantaneous geomagnetic activity as IAR are not visible in spectrograms when geomagnetic activity is high. We find cases where the difference in measured and modeled  $\Delta f$  is significant, suggesting that the model does not capture short term variations in plasma mass density that influence the IAR during these days. We plan to undertake further modeling of  $\Delta f$  on shorter timescales.

**Plain Language Summary** Ionospheric Alfvén Resonances occur when waves traveling along magnetic field lines in the ionosphere are reflected at boundaries where the change in the velocity of the wave reaches a maximum. These waves are observed in data from Eskdalemuir Geophysical Observatory. We have modeled the frequency of these waves and compared this with a 9-year data set we obtained from Eskdalemuir, enabling us to examine trends and increase our understanding of their behavior. We found that the data and the model both reach higher frequencies during the night, winter and during years when the Sun is less active. We compared the frequencies of the Ionospheric Alfvén Resonances with models of electron density in the ionosphere and found that the frequencies are higher when the density of the electrons is lower. We found cases where the frequencies in the data do not match with the frequencies in our model and so we plan to investigate these in further studies.

## 1. Introduction

Ionospheric Alfvén Resonances (IAR) are generated when Alfvén waves traveling parallel to the Earth's magnetic field lines are partially reflected at boundaries in the ionosphere where there are large changes in plasma mass density. These boundaries, which are located above the F-region peak and toward the bottom of the ionosphere, cause the Alfvén velocity gradient to reach a maximum. This process sets up a resonance in the ionospheric cavity centered on the F-region, which was first proposed by Polyakov (1976). Several mechanisms for the production of IAR have been considered, including the ionospheric feedback instability at higher latitudes (Lysak, 1991). Other energy sources, for example, electromagnetic energy from terrestrial lightning strikes, have been suggested (Belyaev et al., 1989; Füllekrug et al., 1998).

IAR can be observed using induction coil magnetometers, especially induction coils with noise levels of better than  $0.1 \text{ pT}/\sqrt{\text{Hz}}$ , in the 0.5–30 Hz range. Their existence was first measured and confirmed by Belyaev et al. (1989) at mid-latitudes, and have since been found as spectral resonance structures in magnetometer data at high (Belyaev et al., 1999; Hebden et al., 2005; Yahnin et al., 2003), mid (Potapov et al., 2014; Molchanov et al., 2004) and low latitudes (Bösinger, 2002; Nosé et al., 2017). In these studies, generally the IAR occur during the nighttime and the frequencies increase from dusk to local midnight and then decrease from midnight to dawn. The frequency range ( $f$ ) of IAR harmonics is usually between 0.5 and 10 Hz (Belyaev et al., 1989). The harmonic frequency separation ( $\Delta f$ ) is often used to describe the behavior of IAR as the frequency changes over time. This is because

the fundamental harmonic is often obscured in spectrograms by lower frequency pulsations, and the number of harmonics visible varies with time.

IAR have been observed in magnetometer data measured at the Eskdalemuir Geophysical Observatory (51.3°N, −3.2°E), which is situated close to the Scottish-English border, UK. Beggan and Musur (2018) investigated the occurrence of IAR from September 2012–September 2017 and observed that the IAR occur more commonly during winter, although they are also observed in the summer. Beggan and Musur (2018) also found examples of IAR that had unexpected variations in  $\Delta f$ . These included smaller scale changes in the frequencies over time, as well as harmonics of the IAR reaching frequencies of above 30 Hz on some occasions. There were also instances of possible interference of the IAR with Schumann resonances, which are quasi-standing waves in the cavity between the Earth and ionosphere generated by lightning (Schumann, 1952). Beggan and Musur (2018) showed that the IAR at Eskdalemuir are observed in spectrograms during periods of low or medium geomagnetic activity.

The study completed by Beggan and Musur (2018) suggested that modeling of the IAR at Eskdalemuir was needed in order to understand the IAR behavior, and to understand the relationship between IAR frequencies and parameters such as  $f_oF2$ , the critical frequency of F2 layer of the ionosphere. The variation of the IAR frequencies at Eskdalemuir over yearly and short term timescales has not been studied and so to further understand the IAR we have obtained  $\Delta f$  from the Eskdalemuir data over the period 2013–2021.

To investigate the frequencies of the IAR at Eskdalemuir, we have created a long-term climatological model of  $\Delta f$ . The model includes hourly Alfvén velocity height profiles, as the Alfvén velocity varies with altitude due to the changing plasma mass density, which we modeled using the International Ionosphere (IRI) (Bilitza et al., 2017). We modeled the magnetic field strength using the International Geomagnetic Reference Field (IGRF) (Alken et al., 2021). We also consider other models of electron density profiles such as the E-CHAIM model (Themens et al., 2017) which is optimized for the ionospheric behavior at higher latitudes, and an ionosonde data driven model.

Here we present a statistical analysis of nine years of  $\Delta f$  from the Eskdalemuir data set of 2013–2021, alongside comparisons of modeled  $\Delta f$  from the IRI, E-CHAIM and ionosonde models. In Section 2 we obtain  $\Delta f$  from the Eskdalemuir magnetometer data, while in Section 3 we model  $\Delta f$  using a time of flight calculation. In Section 4 we make comparisons between the model and data, and discuss these results, and conclude in Section 5.

## 2. Data

The Eskdalemuir Magnetic Observatory is located at a geomagnetic latitude of 57.5°N and a geomagnetic longitude of 83.3°E at an L-shell of  $\sim 3.2$  in 2022. There are two induction coil magnetometers, channel 1 (orientated to geographic north) and channel 2 (oriented to geographic east). The instruments and recording systems were installed by the British Geological Survey Geomagnetism team in summer 2012 with data available from September onwards (British Geological Survey Geomagnetism, 2022). Overall data availability is 95% with short gaps or missing data due to occasional equipment failure.

An example day of data is shown in Figure 1. The magnetometer data are plotted as a spectrogram, from 12:00 UT on 05/03/2013 to 12:00 UT on 06/03/2013. The local time at the Eskdalemuir magnetometer site is approximately equal to UT (longitude −3.2°E). The data have been processed in a similar way to Beggan and Musur (2018). For each day, a five pole Butterworth bandpass filter is applied to the calibrated data, to attenuate frequencies below 0.1 Hz and above 20 Hz. A fast Fourier transform (FFT) with a Hanning window is applied, with a length of 4,096 points. Each FFT consists of 100s of data, with a 100 points between each window. This results in 864 frequency versus power spectra for each day, which are plotted as a spectrogram.

The data in Figure 1 show a typical occurrence of IAR, with the harmonics being visible as bright (i.e., higher power) fringes during the nighttime. Here, the IAR are visible from around 19:00 to 02:00 UT in the frequency range of approximately 0.5–7 Hz.  $\Delta f$  which has been extracted using the method outlined below is plotted in red, with higher orders (2, 3, 4  $\times \Delta f$ ) also plotted.

The first Schumann resonance is also visible at around 8 Hz as a diffuse horizontal band. Other features include narrow subharmonics of the UK power system at 5 Hz which leak in slightly despite the 50 Hz filtering, and vertical lines which indicate lightning strikes within about 2,000 km distance. Below 0.5 Hz there is the standard

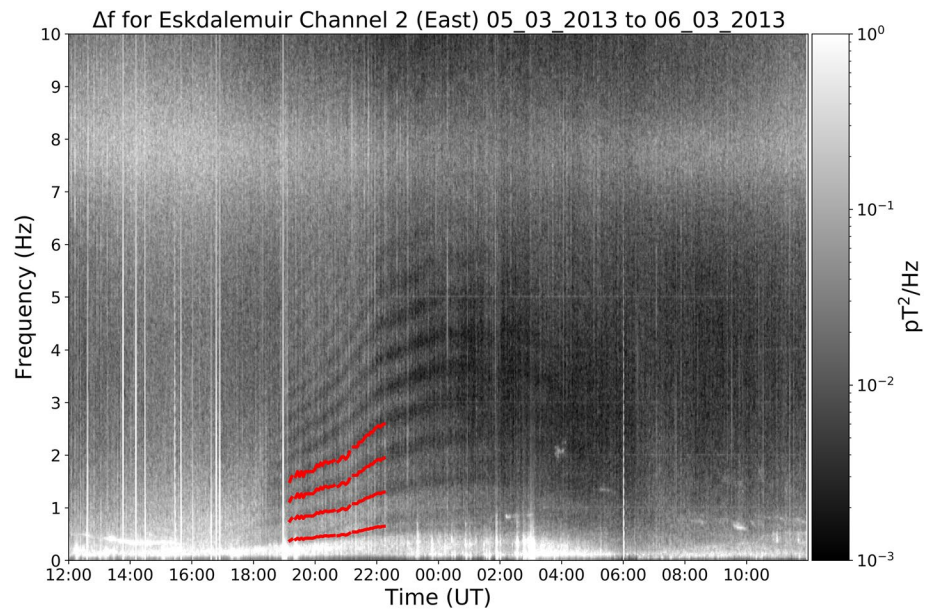


**Figure 1.** Eskdalemuir Channel 2 (East-West) spectrogram from 12:00 UT on 05/03/2013–12:00 UT on 06/03/2013. The IAR harmonics appear as bright fringes from around 19:00–02:00 UT in the frequency range of approximately 0.5–7 Hz.  $\Delta f$  (obtained after IAR are identified by the method of Marangio et al. (2020), see text for details) is plotted in red, with higher orders being plotted ( $2 \times \Delta f$ ,  $3 \times \Delta f$  and  $4 \times \Delta f$ ).

higher intensity, lower frequency activity from the external magnetic field, which tends to obscure the fundamental of the IAR.

The IAR fringes appear more strongly in channel 2 (CH2) and so we chose this magnetometer data set to focus our analysis on. We examined the complete years of 2013–2021, so that we could undertake a statistical analysis on IAR  $\Delta f$  with solar activity and seasonal variability over the 9 years.

Previously,  $\Delta f$  values have been extracted from data manually, such as by using cursor clicking methods (Hebden et al., 2005).  $\Delta f$  has been semi-automatically extracted by Odzimek et al. (2006), where IAR are first detected and then a fitting method is used to find  $\Delta f$ . Molchanov et al. (2004) used a semi-automatic method to obtain  $\Delta f$  for 2.5 years of data by performing a Fourier transform of the data and calculating the difference between the peaks in frequency. Beggan (2014) used a peak finding algorithm to identify IAR fringes. Nosé et al. (2017) extracted  $\Delta f$  by detecting peaks in power spectra and confirming the results visually.

More recently, Marangio et al. (2020) used machine learning techniques to identify the IAR. To automatically detect IAR in the data we used this machine learning method to identify the IAR in spectrograms. This method employs a U-Net, a fully convolutional neural network (Ronneberger et al., 2015), which does not require a large training set. We follow the method provided by Marangio et al. (2020). To train the model, we tried a variety of training sets consisting of manually drawn labels from our spectrograms, manually drawn labels from the Marangio et al. (2020) data set and labels generated automatically by Beggan (2014). The best results were returned using a mixture of all labeled data. Using grayscale images only, we adjusted the brightness limits of the spectrograms so that the IAR fringes were most visible. Our final training set consisted of 278 images with identified and labeled IAR fringes.

The method given by Marangio et al. (2020) used a time range of 06:00–18:00 UT but suggested that spectrogram images covering a wider time range could be used. However, when using a time range of 24 hr the U-Net did not train correctly; the output images were blank and no IAR were identified. At frequencies lower than 0.5 Hz the IAR are obscured by lower frequency activity and at frequencies above 6.5 Hz the Schumann resonance is detected but misidentified as IAR. We found that the U-Net could detect IAR best when the time range was between 16:00–08:00 UT, as the IAR appear in the spectrograms during nighttime hours. We set the frequency range of 0.5–6.5 Hz to exclude the first Schumann resonance. The output from the U-Net consists of images with probability values of each pixel of being an IAR ranging from 0 (not IAR) to 1 (IAR). The output pixel values

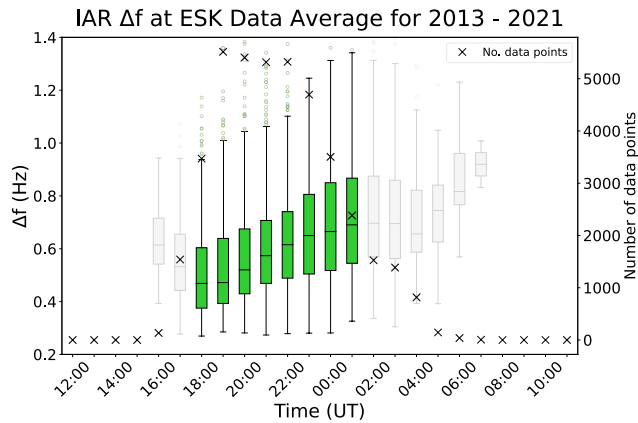


**Figure 2.** A boxplot of the U-Net detected IAR  $\Delta f$  (left-hand scale) at Eskdalemuir, for 2013–2021. The black crosses (right-hand scale) mark the number of data points in each hour. Green shaded time bins are where the number of data points is above 2,090.

are continuous (as expected) and so we apply thresholds to find the optimal selection of IAR. We found a threshold of 0.7 visually matches the manually identified IAR while reducing the impact of spurious non-IAR features. Examples of output and thresholded images can be viewed in the Marangio et al. (2020) paper.

Once the U-Net has been trained, classifying IAR in an input image is very quick ( $\ll 1$  s). We computed a spectrogram with the same time and frequency range as the training set for each available day in the magnetometer data set covering 2013–2021 and applied the trained U-net model to identify the harmonics.

The U-Net output images consist of  $256 \times 256$  pixels of frequency versus time. By finding the average difference between the maximum peaks in each time bin of the image, we obtained the average  $\Delta f$  for each time bin of pixels. In order for  $\Delta f$  to be calculated, we used a minimum of 4 peaks (corresponding to 4 harmonics) in each time bin to minimize false positive IAR and avoid gaps in the data where possible. Hence, we automatically calculated  $\Delta f$  for the full data set and obtained a  $\Delta f$  value every 3.75 min (16 pixels per hour). In order to check these results, we plotted  $\Delta f \times n$  where  $n$  is an integer onto the original spectrogram, and we found that the  $\Delta f$  values follow the shape

of the IAR harmonics, which is apparent in Figure 1 (shown in red). The red lines do not lie on top of the bright fringes of the harmonics in the spectrogram, although the harmonic separations match well. This is a consequence of simply overplotting  $\Delta f$ ,  $2 \times \Delta f$ ,  $3 \times \Delta f$ , and  $4 \times \Delta f$  on the spectrogram. However the resonator is not homogeneous, as discussed in Section 3, which results in a deviation of  $\Delta f$  for the lowest harmonic (Potapov et al., 2022), and so there is an offset between the bright fringes in the spectrogram and the overplotted red  $\Delta f$  lines.

In Figure 2 we plot the resulting  $\Delta f$  values as a boxplot, with a bin for each hour. As there are up to 16 data points in a given hour, we found the mean  $\Delta f$  value for each hour of each day in the data set. We combined these hourly averages for the years 2013–2021. The horizontal line in each box is the median value of  $\Delta f$  for each hour. The lower and upper boundaries of each box are the first and third quartiles of the frequencies, with the whiskers being 1.5 times the inter-quartile range. Circular points show outliers. The frequency on the y-axis has a limit of 1.4 Hz so that it can be comparable to other plots and any data points above this value are not included here.

The black crosses show the total number of data points in each bin. The standard deviation of the number of hourly binned data points is 2,090. The bins shaded in green contain a total number of points greater than this standard deviation, which are contained in the time range 18:00–01:00 UT. Other hour bins are grayed out as we assessed there are insufficient data available to make a good statistical analysis during these UTs.

Table 1 summarizes the number of data points for each month of each year. This table shows the number of times that the U-Net has identified the IAR. Each point represents a pixel in the output U-Net image. Each hour contains 16 pixels.

### 3. Modeling of IAR Climatology

Lysak (1993) previously modeled the IAR and included the parallel electric field associated with the IAR finding that the frequencies scale with  $V_A/2h$  where  $V_A$  is the Alfvén velocity in the ionosphere and  $h$  is the scale height of the ionospheric density. This follows the widely used model from Polyakov and Rapoport (1981) which has been used by many others to estimate  $\Delta f$  and its properties at different latitudes (Hebden et al., 2005; Nosé et al., 2017).

As a starting point, the International Reference Ionosphere (IRI) (Bilitza et al., 2017) is often used to parameterize the conditions of the IAR cavity (Potapov et al., 2014; Nosé et al., 2017; Yahnin et al., 2003), specifically the plasma mass density as this strongly controls the frequencies of the IAR due to its effect on the Alfvén velocity. For example, Potapov et al. (2014) used a time of flight approach alongside the IRI-12 and International Geomagnetic Reference Field (IGRF-11) to model  $\Delta f$  for 13 days at mid-latitude observatory (Mondy;  $L = 2.1$ ) and found high correlation between measured and observed values.

We have used a similar approach as outlined below. However, as we have an observed  $\Delta f$  value every 3.75 min for 9 years (where IAR are detected), we modeled  $\Delta f$  for every hour. This large data set provides a new insight into

**Table 1**

Number of Data Points for Each Month of Each Year, Corresponding to the Number of Times the U-Net has Detected an IAR Pixel

	January	February	March	April	May	June	July	August	September	October	November	December
2013	254	226	722	503	202	112	176	637	1,207	968	681	28
2014	444	336	337	166	175	116	190	659	674	543	170	123
2015	566	499	448	230	201	138	127	424	876	491	318	46
2016	195	325	593	623	559	482	769	773	414	362	325	256
2017	161	105	276	533	401	376	466	800	230	367	255	7
2018	232	210	188	586	614	622	818	501	417	474	126	70
2019	112	141	316	512	566	716	540	440	482	129	84	180
2020	106	85	368	551	483	544	518	445	519	381	203	79
2021	64	123	196	550	794	570	514	217	331	468	381	70

Note. Total number of data points is 41,302.

the behavior of the IAR. To model the IAR  $\Delta f$  at Eskdalemuir, we calculated the time of flight,  $T_f$ , for an Alfvén wave to travel up and down the IAR cavity and set  $\Delta f = 1/T_f$ . The time of flight is:

$$T_f = 2 \int_a^b 1/V_A dl. \quad (1)$$

The Alfvén velocity,  $V_A$ , is given by:

$$V_A = \frac{B}{\sqrt{\mu_0 \rho}} \quad (2)$$

where  $B$  is the magnetic field strength (in Tesla),  $\rho$  is the plasma mass density ( $\text{kg m}^{-3}$ ) and  $\mu_0$  is the permeability of free space ( $\text{H m}^{-1}$ ). The integral limits  $a$  and  $b$  are the bottom and top boundaries of the IAR cavity. The Alfvén velocity varies primarily because the plasma mass density changes rapidly with altitude.

To model the plasma mass density, we assumed quasi-neutrality. The IRI, which includes solar, magnetic and ionospheric indices, gives altitude profiles of ion composition percentages and electron density, from which plasma mass density can be calculated. Values are provided for an altitude range of 80–2,000 km. We computed a value for the plasma mass density every 10 km along the field line over Eskdalemuir, for any given hour. As well as using the IRI to obtain electron density profiles, we also modeled electron density using the Empirical-Canadian High Arctic Ionospheric Model (E-CHAIM) and ionosonde data, as outlined below.

E-CHAIM is designed to better model the ionosphere at higher geomagnetic latitudes of 50°N and above, and provides electron density profiles (Themens et al., 2017, 2018, 2019). As Eskdalemuir is located at a geomagnetic latitude of 57.5°N, we created a model of plasma mass density using electron density profiles from E-CHAIM (v3.1.4, with Storm NmF2 enabled and auroral module not enabled, as recommend by default) combined with ion compositions from the IRI, as described above.

The critical frequency of the F2 layer of the ionosphere ( $foF2$ ) is related to the peak electron density,  $N_e$ , by  $foF2 = 8.98 \times \sqrt{N_e}$ . To obtain a data driven model of electron density, we used ionosonde data. The closest ionosonde to Eskdalemuir is the Chilton ionosonde (RAL Space, UKSSDC, 2022), which is located 3.7° south of Eskdalemuir (at 51.70°N, 358.67°E). We ran the IRI model at the location of Chilton to get  $foF2$  and found the difference between this modeled  $foF2$  and the  $foF2$  measured by the ionosonde. From this, we calculated the perturbation of the peak electron density between the IRI and ionosonde which is  $1 + ((Chilton_{N_e} - IRI_{N_e})/IRI_{N_e})$ . We applied hourly perturbations to the IRI electron density profiles at the higher latitude of Eskdalemuir, resulting in adjusted plasma mass density profiles. This created three separate models of plasma mass density; one modeled solely using the IRI, one with using E-CHAIM for the electron density profile and one using the IRI electron density profile adjusted with the Chilton perturbation.

We used the International Geomagnetic Reference Field (IGRF-13) (Alken et al., 2021) to compute the field line location and model the magnetic field strength along it. The magnetic field lines have curvature and so we

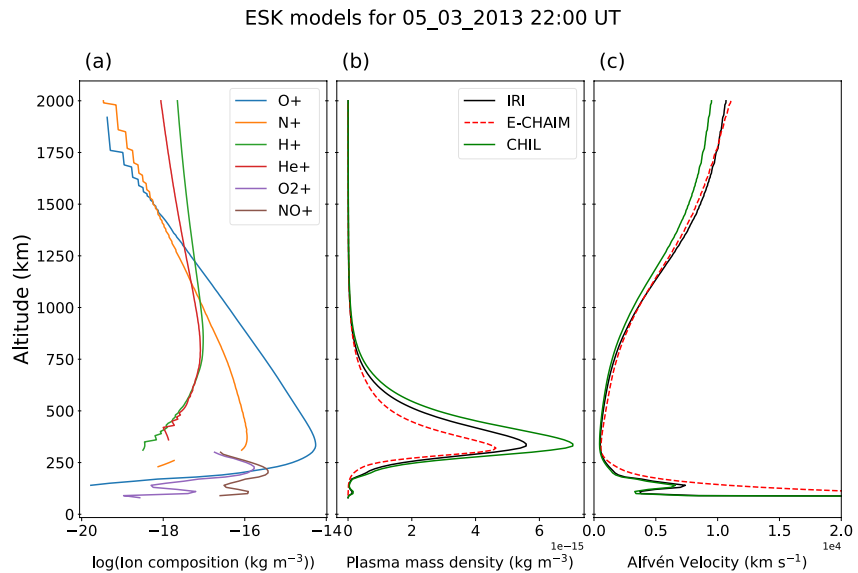


**Figure 3.** Models of (a) log of ion compositions modeled by the IRI, (b) plasma mass density profiles and (c) resulting Alfvén velocity profiles ( $x$ -axis limit of 20,000  $\text{km s}^{-1}$ ) for 22:00 UT on 05/03/2013. Plasma mass density and Alfvén velocity profiles are plotted for the IRI (black), E-CHAIM (red) and Chilton adjusted (green) models.

considered the angle of the field line when finding magnetic field strength. IGRF field lines are not traced at constant separations, hence we interpolated over the field lines to points in altitude coincident with the IRI location. The angle of a magnetic field line ( $\theta$ ) is given by:

$$\tan \theta = \frac{(B_x^2 + B_y^2)^{1/2}}{B_z}$$

where  $B_x$ ,  $B_y$ , and  $B_z$  are the components of the magnetic field at the given location.

The actual distance the wave travels up the field line for each increment is given by  $L = 10 \text{ km}/\cos\theta$ . We found the  $1/\cos\theta$  term does not vary significantly, given the high magnetic inclination, but is included in our model of the magnetic field strength for completeness.

We next calculated the Alfvén velocity using the plasma mass density profiles and the magnetic field strength, resulting in three modeled Alfvén velocity profiles for a given hour. The models have values covering 80–2,000 km; however the Alfvén velocity reaches a maximum above the F-region peak so if the cavity size is greater the additional time taken for the wave to propagate to the upper boundary is negligible. Likewise, the Alfvén wave will become a free-space electromagnetic wave below the ionosphere and so will reach velocities up to the speed of light. Therefore, we are justified in using the cavity size allowed by the IRI. From the Alfvén velocity profiles we computed the time taken for the wave to travel up and down the cavity, using the lower boundary to be 80 km and the upper boundary to be 2,000 km (corresponding to integral limits  $a$  and  $b$  in Equation 1), from which we modeled a value for the expected  $\Delta f$  for each hour.

The modeled ion compositions, plasma mass density profiles and Alfvén velocity profiles for 05/03/2013 at 22:00 UT are presented in Figures 3a–3c. In panel (a), the log of the ion compositions are plotted, which are scaled with the IRI electron density profiles. The most dominant ion in this case is O+. The same percentage ion compositions are used in all three models. In panel (b), the plasma mass density profiles are plotted. The solid black line is the IRI model, where the percentage ion compositions are scaled with the IRI electron density models. The red dashed line is the E-CHAIM model, in which the percentage ion compositions are scaled with the E-CHAIM electron density profile. The green line is the Chilton adjusted model, where the perturbation between the ionosonde measured peak electron density and the IRI modeled peak electron density is applied to the electron density profile that scales this model. The Alfvén velocity profiles are plotted in panel (c), demonstrating the non-uniformity of the IAR cavity. The Alfvén velocity gradients reach a maximum above the F-region and toward the bottom of the ionosphere. Hence, the time of flight of the wave within these boundaries is most

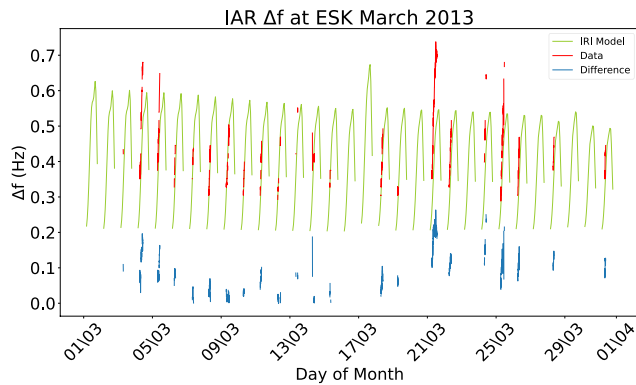


**Figure 4.** Modeled  $\Delta f$  values at Eskdalemuir using the IRI are plotted in green for each day of March 2013, from 16:00–08:00 UT. IAR values extracted from the U-Net are shown in red. The absolute difference between the model and measured data is plotted in blue.

important in modeling  $\Delta f$ . Using the limits given by the IRI (80–2,000 km) encompasses the region which controls the IAR  $\Delta f$ . These different Alfvén velocity profiles lead to different modeled values of  $\Delta f$ .

As an example, Figure 4 presents the IRI  $\Delta f$  model and  $\Delta f$  extracted from the data for March 2013. For hours 16:00–08:00 UT, the modeled values are shown in green and the data are plotted in red. The absolute difference is plotted in blue. Here, the model and data show similar daily variation in  $\Delta f$  however there is a larger increase in  $\Delta f$  on 21/03/2013, suggesting that the IRI does not accurately reflect the conditions of the ionosphere on this day. A large geomagnetic storm took place on the 17 March 2013 which had significant and long lasting ionospheric disturbances (Yue et al., 2016). This may have had further effects on the IAR  $\Delta f$ .

## 4. Results and Discussion

Figure 5 presents the full models for 2013–2021 as boxplots of hourly  $\Delta f$  values. Figure 5a shows the IRI model, (c) shows the E-CHAIM model and (e) shows the Chilton model. All models reveal an increase in frequency

during the nighttime hours, however there is a decrease in the frequency just after midnight for the IRI and Chilton models. This feature is most visible in the winter months of the model.

Figure 5b IRI model, 5d E-CHAIM and 5f Chilton model, show boxplots of the portion of the modeled  $\Delta f$  values which correspond to times where the U-net has detected IAR and hence there are  $\Delta f$  values from the data. We call these "reduced" models as they only contain  $\Delta f$  values when IAR were detected in the spectrograms. Therefore, figures showing the reduced models can be directly compared to Figure 2, which shows the data.

In the reduced models, we see a more similar structure to that in the data compared to the full model plots. By looking at this selection of the model, the double peak feature, which is clear in the winter months of the full models, is removed. This could suggest a sampling bias effect and that the U-Net is detecting fewer instances of IAR in the winter, although previously Beggan and Musur (2018) found more occurrences of IAR in the winter. This is discussed in Section 4.1.

We calculated the percentage difference between the extracted IAR  $\Delta f$  values and each version of the model, as shown in Figure 6. Note the x axis limit is 80%. The black line shows the IRI model, the red line shows the E-CHAIM model and the blue line shows the Chilton model. From this analysis we see that in general, all three models tend to underestimate  $\Delta f$ . This may be caused by the models overestimating electron density, or that the time of flight treatment is not fully capturing the behavior of the IAR.

The absolute median percentage difference is 19% for the IRI model, 20% for the E-CHAIM model and 22% for the Chilton model.

Previously Yahnin et al. (2003) compared  $foF2$  measurements with IRI electron density at high latitude at the same observatory site as the magnetometer and modeled  $\Delta f$ . They found an improvement in this model in comparison to the model which used IRI electron density profiles. The poorer performance of the Chilton model suggests that, although it is data driven, the latitudinal distance between Chilton and Eskdalemuir may be too great. Perturbations in the ionosonde data could be caused by traveling ionospheric disturbances such as Atmospheric Gravity Waves (AGWs). Therefore a time shift to the Chilton perturbations would need to be applied at Eskdalemuir for cases where an AGW could have occurred. A more careful analysis is needed to investigate this further.

Given the IRI model is statistically the most accurate, for the remainder of this paper we use it in comparisons with the IAR data.

### 4.1. Seasonal Variation

Figures 7a–7c show the seasonal variation of  $\Delta f$  for the IAR data, IRI model and reduced IRI model. The four lines represent the four seasons, with each year being split up relative to the equinoxes and solstices. We have defined winter as November–January (blue), spring as February–April (red), summer as May–July (black) and

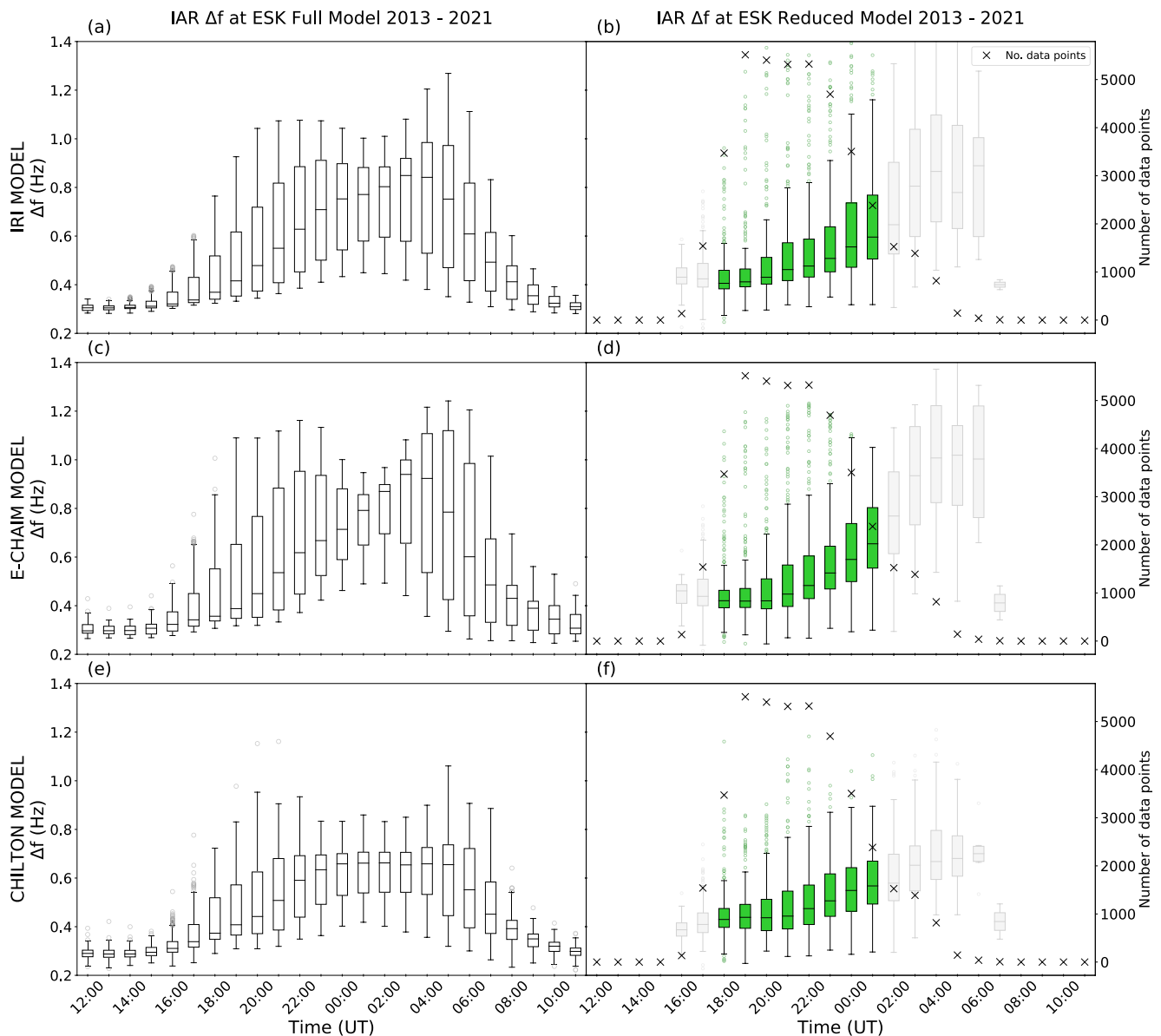


**Figure 5.** Boxplots of various models of the  $\Delta f$  at Eskdalemuir, for 2013–2021. The left-hand column shows the ionospheric model outputs using all days: (a) uses the IRI to model electron density, (c) uses E-CHAIM to model electron density and (e) uses IRI electron density profiles modified in relation to Chilton  $foF2$  data. The right-hand column shows reduced versions of these models to include times only where there are IAR data, plotted in the same format as Figure 2 ((b) IRI model, (d) E-CHAIM model, (f) Chilton model).

autumn as August–September (green). For each season, the average value for each UT is plotted. In the data (a) and reduced model (c), UTs outside the range 18:00–01:00 UT are grayed out as they do not have enough data points to be considered in the analysis.

In both the data and the model, the winter months (blue) have the highest  $\Delta f$  values and the summer months (black) have the lowest. This is consistent with previous studies of IAR at high and mid latitude. At high latitude ( $L = 5.2$ ), Yahnin et al. (2003) examined a data set from June 1995 to December 1999. IAR occurred more in the winter months and  $\Delta f$  was also greater. At mid latitude ( $L = 2.1$ ), Potapov et al. (2014), whose data set consisted of 100 hr of data from March 2010 to May 2011 also found that  $\Delta f$  was greatest in the winter. However they did not find that occurrence had any seasonal dependence.

In the Eskdalemuir data set, there were the least number of data points in the winter and the most number of points in autumn months. This is because the U-Net detected the most IAR during the autumn. Previously,

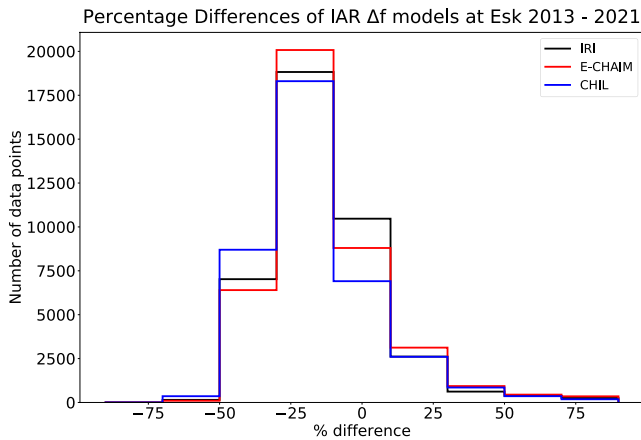


**Figure 6.** A histogram of the percentage differences between the IAR  $\Delta f$  models and the IAR  $\Delta f$  data for 2013–2021. The percentage difference is calculated by  $((\text{model}-\text{data})/\text{data})$ . The model using the IRI for electron density is in black, the model using E-CHAIM for electron density is in red, and the model using the Chilton ionosonde data adjusted IRI for electron density is in blue. All three models use the IRI for ion composition and the IGRF for magnetic field strength. Bins are given in widths of 10% and the number of data points in each bin is shown on the y-axis. The x-axis shows the percentage difference and has limits of  $-80\%$  and  $80\%$ .

Beggan and Musur (2018) examined the occurrence of IAR at Eskdalemuir for 5 years between 2012 and 2017 and found that the IAR occur most during the winter months. In our case, it is likely that the U-Net did not detect as many instances of a positive IAR identification during the winter because the fringes of the harmonics in the spectrograms are not as bright during the winter, and are more diffuse, which makes them more difficult for the U-Net to detect.

In the model (Figure 7b), there is a decrease in  $\Delta f$  in the winter months after midnight. This comes from an increase in the modeled electron density, where we found that there is an increase in density around midnight. This is due to the semidiurnal component of  $f_oF2$  at mid-latitudes, which occurs during the winter time (Zolotukhina et al., 2014). At around midnight, there is an increase in peak electron density. This is not as apparent in the data (Figure 7a), which may be due to lack of winter data points. However, between 00:00 UT and 04:00 UT there is a decrease in  $\Delta f$  in the winter, which then increases again afterward. This may be an indication of the semidiurnal component of  $f_oF2$  which is seen in the model. We plan to investigate this in further study.

When directly comparing the data and reduced model, the reduced model has lower  $\Delta f$  values than the data in the spring, summer and autumn months; the model is underestimating  $\Delta f$  during these seasons. However, in the winter months, the reduced model has greater  $\Delta f$  values than the data, and so it is overestimating  $\Delta f$ . The mean difference between the average UTs

(18:00–01:00 UT) of reduced model and data is greatest in the winter and autumn at approximately 0.1 Hz, and lowest in the spring and summer at around 0.08 Hz. Interestingly, at low latitude ( $L = 1.3$ ), Bösinger (2002) examined a data set consisting of half a year of measurements from 1999 to 2000 observed that there was more variability in  $\Delta f$  during the winter. However, when they used the IRI to compute expected  $\Delta f$ , this variability was not reflected in the model.

## 4.2. Yearly Variation

The average UT hourly values of  $\Delta f$  for each year for the data, model and reduced model are plotted in Figures 8a–8c. For the data and reduced model, we have included averages in the time range 18:00–01:00 UT. In both the data and the model, the years 2017–2020 have the greatest  $\Delta f$  and 2013–2015 have the smallest  $\Delta f$ . This is discussed in more detail in relation to the solar cycle in the next section. In the model (Figure 8b) there is a larger difference in  $\Delta f$  for years 2013, 2014, and 2015, which have the lowest frequencies, compared to the other years. This is not as apparent in the data (Figure 8a).

When comparing the reduced model (c) with the data (a), we found that the mean yearly difference between the reduced model and data ranges between 0.07 and 0.12 Hz (for 18:00–01:00 UT), suggesting that on yearly timescales, the model works well.

## 4.3. Comparison With Geomagnetic and Ionospheric Indices

### 4.3.1. $f_oF2$

As the IAR  $\Delta f$  is related to plasma mass density by the Alfvén velocity, as outlined in Section 3, we now examine any correlation between  $\Delta f$  and  $f_oF2$ . We obtained  $f_oF2$  values from the Chilton ionosonde (which is at a slightly lower latitude compared to Eskdalemuir), as before, for every data point. Figures 9a–9c show boxplots for  $f_oF2$  with the data, model and percentage difference between data and model. Each  $f_oF2$  bin contains the same number of data points. Times where the corresponding  $f_oF2$  measurement was bad (flagged in the ionosonde data as 99.99) have been removed. The maximum frequency on the plots is capped at 1.4 Hz for ease of comparison between the model and the data, which removes some outliers. These are also not included in the total number of points.

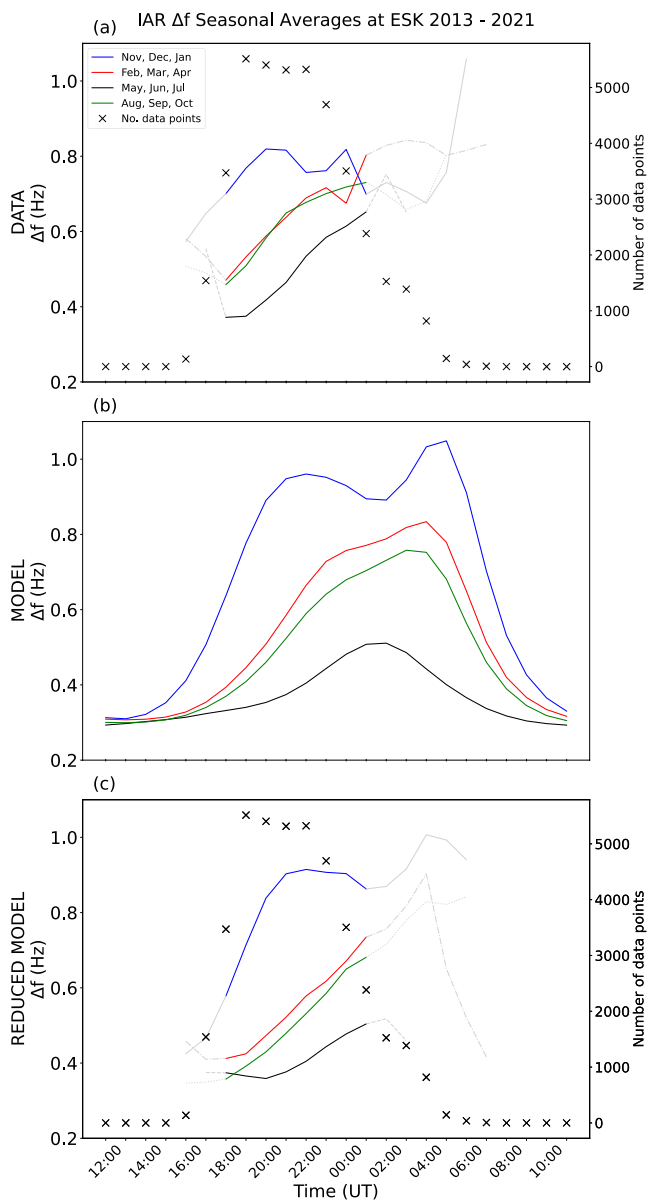


**Figure 7.** Average hourly IAR  $\Delta f$  data (a), model (b), and reduced model (c) for each season. Winter months (November, December, and January) are in blue, spring months (February, March, and April) are in red, summer months (May, June, and July) are in black and autumn months (August, September, and October) are in green. The black crosses mark the number of data points. Hourly averages outside the time range of 18:00–01:00 UT have been grayed out as they do not have a significant number of data points.

From these figures we see that there is an inverse correlation between  $\Delta f$  and  $foF2$ , so the IAR have greater  $\Delta f$  values when  $foF2$  is lower. Although Beggan and Musur (2018) found little correlation between  $foF2$  and IAR  $\Delta f$  for six Eskdalemuir case study days where the behavior of the IAR was unusual, we find that when considering the 9 year data set as a whole, there is clear anticorrelation. This follows the results of Potapov et al. (2014), in which an anticorrelation was also found.

### 4.3.2. SYM-H and Kp

SYM-H is a geomagnetic index which is used to describe the ring current. We used OMNI data (King, 2005) which gives SYM-H in a 1 min cadence. We analyzed the Eskdalemuir data set in comparison to the SYM-H data set in a similar way to our analysis of  $foF2$ .

In the IAR data set the corresponding values of SYM-H range from  $-53$  to  $44$  nT. Most of the times when IAR have been identified correspond to SYM-H values between  $-16$  and  $8$  nT. There are more  $\Delta f$  data points centered around  $0$  nT, which correspond with lower geomagnetic activity. There are no extreme values of SYM-H and hence no large geomagnetic storms. Comparing the reduced model and SYM-H reveals no clear correlation of  $\Delta f$  with SYM-H. During high geomagnetic activity, when SYM-H is expected to be at more extreme values, the spectrograms are saturated with high intensity activity. Therefore, any IAR that are present will be obscured and so not visible in the data.

Kp (planetary index) is a geomagnetic index which has a value every 3 hr (Matzka et al., 2021). We obtained Kp values (from the GFZ German Research Centre for Geosciences) so that we had a corresponding Kp value for each data point.

The Kp index ranges between 0 and 9. The National Oceanic and Atmospheric Administration (NOAA, 2022) defines a minor geomagnetic storm as having a Kp of 5. In our data, most of the  $\Delta f$  data points occur with a Kp index of 0.67 and the greatest Kp value is 4, which corresponds to low geomagnetic activity. For the 5 years of Eskdalemuir data Beggan and Musur (2018) analyzed, the IAR occurred at Kp values of 4 and below. Our study confirms this is the case for the 9 year data set of 2013–2021. Most of the  $\Delta f$  data points occurred at a Kp of 0.67, after which the number of data points decreases. This suggests an anticorrelation of the U-net detecting IAR and Kp index. Previous studies across a range of latitudes (Belyaev et al., 1989; Yahnin et al., 2003; Hebden et al., 2005; Potapov et al., 2014; Nosé et al., 2017) found an anticorrelation of IAR occurrence and Kp.

The  $\Delta f$  values in both the data, model and percentage difference plots do not have a correlation with Kp, suggesting that at low levels, geomagnetic activity does not affect the frequencies of the IAR harmonics.

The IAR at Eskdalemuir have been identified by the U-Net at times during low geomagnetic activity for both SYM-H and Kp, and there is no visible correlation between  $\Delta f$  and geomagnetic activity (when it is low). During strong periods of geomagnetic activity, IAR are not visible in the Eskdalemuir spectrograms. The high intensity activity may obscure the IAR harmonics and so we cannot be certain whether there is a relation between geomagnetic activity and IAR  $\Delta f$ , however there is no clear correlation with Kp and the IAR  $\Delta f$  that the U-Net has identified. As these parameters did not show any correlation, the data are not presented graphically here.

Parent et al. (2010) analyzed evolution of IAR  $\Delta f$  during a substorm and found that  $\Delta f$  decreased after the substorm event. By looking at digisonde, riometer and all-sky imager data, they suggested that the reason for

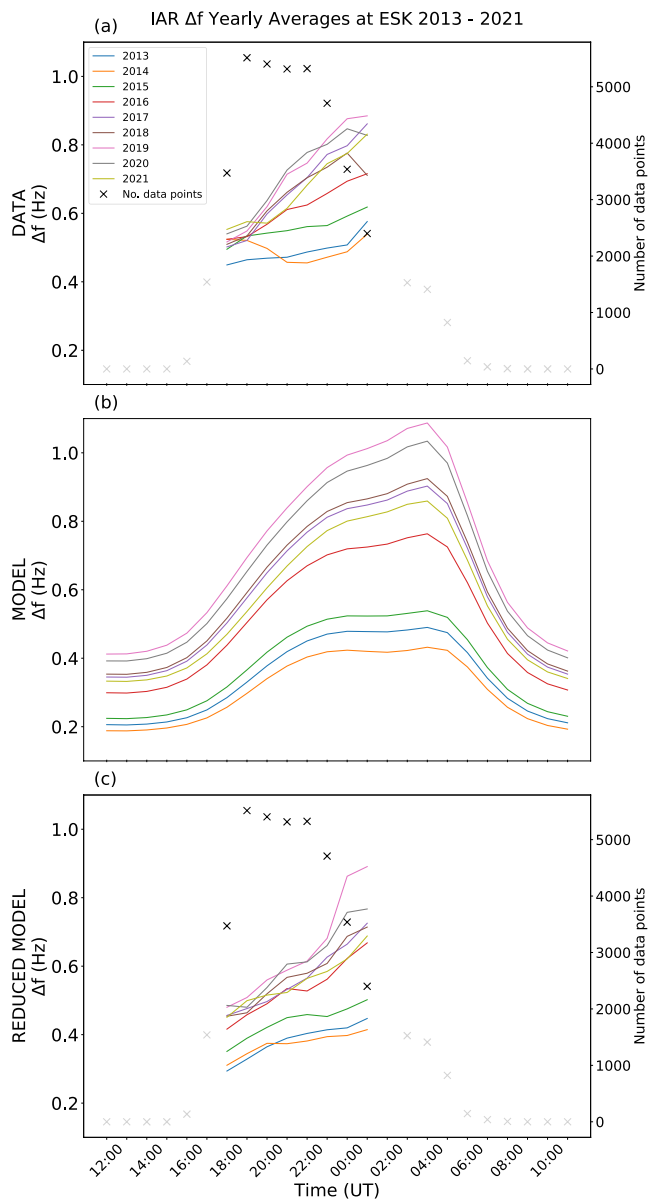


**Figure 8.** Average hourly IAR  $\Delta f$  data (a), model (b), and reduced model (c) for each year in the range 2013–2021. Black crosses mark the number of data points. Hourly averages are plotted for the time range 18:00–01:00 UT where there are a significant number of data points.

order to determine if each year of percentage differences are statistically significant from each other. In the test, we compared each year to the full 9 year data set of percentage differences. The results of this significance test showed that the individual years are significantly different to each other, with a small probability that the data for each year could have been randomly sampled from the data set (with a median  $p$  value of  $8.15 \times 10^{-28}$ , close to 0). Hence, as the data are statistically significant, we can be confident in the correlation of the percentage differences of each year and the solar cycle.

The greatest increase in percentage difference occurred between 2015 and 2018, which corresponds to the descending phase of the solar cycle (Jayalekshmi et al., 2022) (descending phase was February 2015–June 2019). The yearly medians increased from 20.6% to 25.9% so the IRI model is the least accurate during this phase. During the descending phase of the solar cycle, there is an increase in geomagnetic activity caused by coronal

this decrease in frequency is because after the substorm, more electrons precipitate into the F-region of the ionosphere and hence the plasma mass density increases, resulting in a decreased  $\Delta f$ . This suggests that the effects of geomagnetic activity may be visible during the days following high activity, and so we would not expect to see an instantaneous or simultaneous correlation between  $\Delta f$  and geomagnetic activity.

### 4.3.3. Sunspot Number

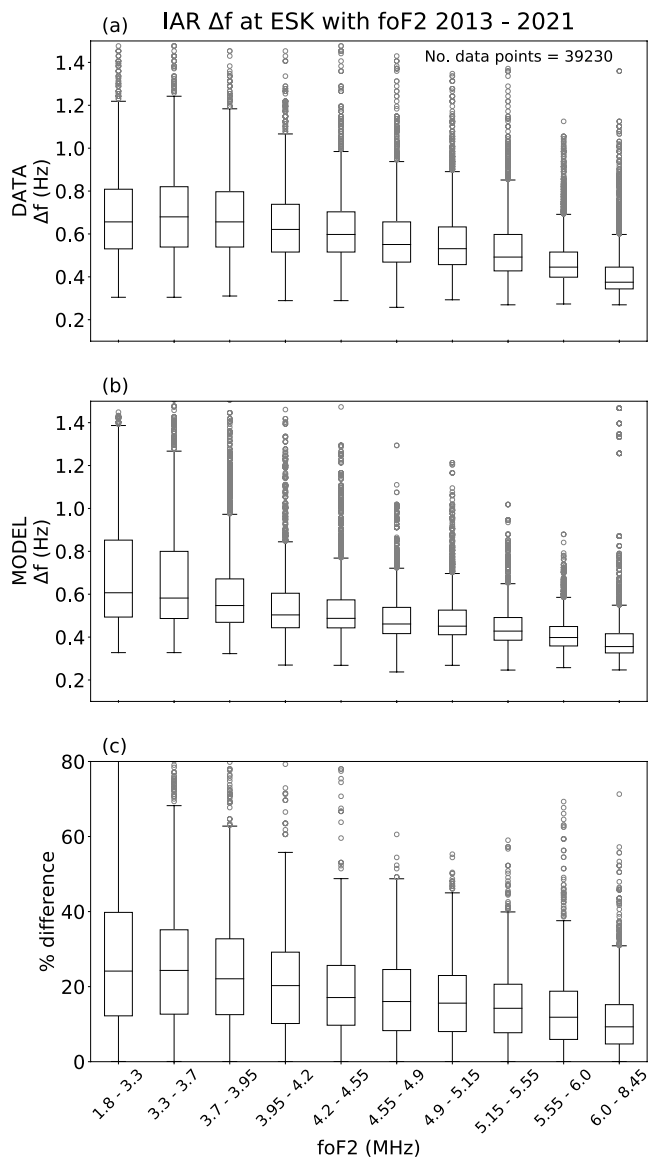
Finally, we compared the data and model with daily sunspot number (SILSO World Data Center, 2013–2021). When looking at daily sunspot number, the  $\Delta f$  data set corresponds to days with sunspot numbers in the range of 0–180 which are relatively low, again suggesting that the IAR are detected at times of low geomagnetic activity. At higher sunspot numbers there may be more storms which will mask possible IAR on the spectrograms. The data set has more instances of IAR being detected during days when the sunspot number is lower. Potapov et al. (2014) found that IAR occur for a longer duration during lower sunspot number and hence it follows that the occurrence as we have defined it is also greater at lower sunspot number.

Figure 10a shows the  $\Delta f$  values from the data for each year plotted with average yearly sunspot number, and Figure 10b shows the same for the reduced model. In both cases, the years 2016–2020 have the highest median  $\Delta f$  values, ranging between 0.57 and 0.62 for the data. These years correspond to the lowest average yearly sunspot numbers, which range from 39.8 to 7.0. The years 2013–2015 have the lowest median  $\Delta f$  values (the data ranges from 0.47 to 0.56) which correspond to greatest average yearly sunspot numbers (94.0–133.3). It is clear from this figure that there is a relationship between sunspot number and  $\Delta f$ , with lower sunspot numbers giving rise to greater  $\Delta f$  values. Sunspot number has a linear correlation with  $foF2$ , hence at lower sunspot numbers and lower  $foF2$   $\Delta f$  is expected to increase as the Alfvén velocity decreases.

In 2013 and 2014, the median  $\Delta f$  values in the data were 0.47 and 0.48 Hz respectively. These are the years with the lowest  $\Delta f$ . In 2015 the median increased to 0.56 Hz, and remained above this value for the remainder of the years. The solar cycle 24 maximum lasted from October 2011 to January 2015 (Jayalekshmi et al., 2022) and so it is expected that  $\Delta f$  will be lower during this time period, as is reflected in both the data and the model.

These results suggest that although the IAR  $\Delta f$  does not change over short timescales with geomagnetic activity, it does reflect the variability with the solar cycle.

Figure 10c shows the absolute percentage differences between the model and data for each year as a boxplot, alongside the corresponding average yearly sunspot number. We conducted a two sample Kolmogorov-Smirnov test in



**Figure 9.** Boxplots of IAR  $\Delta f$  data (a), reduced model (b) with  $foF2$  measured by the Chilton ionosonde. Panel (c) is a boxplot of the absolute percentage difference between the data and modeled  $\Delta f$  values with  $foF2$ , with a y-axis limit of 80%. The binned  $foF2$  ranges include the lowest value and up to but not including the greatest value. Data points corresponding to missing ionosonde data have been removed, resulting in a total number of data points of 39,230.

holes on the Sun (Tsurutani et al., 1995), and so this may suggest that the model does not capture the effects of these on the IAR.

#### 4.3.4. Limitations and Future Work

The aim of this research was to model and investigate the climatology of the IAR at Eskdalemuir. The IRI and E-CHAIM models follow the same seasonal and diurnal trends of  $\Delta f$ . In general, the models tend to slightly underestimate  $\Delta f$ . Although we suggest reasons for this, further investigation is required to understand this discrepancy.

We have observed more rapid changes in  $\Delta f$  which occur on shorter timescales than the expected diurnal variation. These variations are not captured in the models and so next we will examine these as case studies and further develop our understanding of these days, for example, by including the effect of AGWs. Days where the difference between the modeled  $\Delta f$  and the data suggest that the ionosphere may be behaving differently to the IRI model and so it will be beneficial to study these in more detail, for example, by considering possible long term effects of geomagnetic activity following geomagnetic storms.

The  $\Delta f$  data which we extracted from the Eskdalemuir magnetometer data relies on the U-Net's capability of detecting IAR in spectrograms. As the U-Net is most efficient when the IAR appearance is bright (or well above the background), the data set is biased toward the summer months, where the fringes are more intense in the spectrograms. This means our analysis is certainly poorer in winter. As the semi-diurnal feature in  $foF2$  appears strongly in the winter months of the model, we will analyze these months more closely in future studies. To do this we may use a cursor clicking technique to extract  $\Delta f$  during the winter on days where we observe the semi-diurnal feature in the data.

## 5. Conclusions

We have examined the IAR  $\Delta f$  in a nine year data set covering 2013–2021 obtained from Eskdalemuir Observatory, UK. We used a U-Net machine learning algorithm to extract IAR  $\Delta f$ . This method performs best when the IAR are more intense which corresponds to the summer months. The large data set that we obtained allowed us to conduct a thorough study of IAR  $\Delta f$  at a mid-latitude location over most of a solar cycle. At Eskdalemuir, we observed a strong anti-correlation with  $foF2$  and  $\Delta f$ , which follows from theory, as electron density, and hence plasma mass density, strongly controls the IAR frequencies. The IAR identified by the U-net tended to occur during times of low geomagnetic activity.

Our model of the IAR at Eskdalemuir using the IRI and E-CHAIM follows the same general seasonal and yearly trends as the data. In both,  $\Delta f$  increases during the night and is greater during the winter months and during solar minimum. The performance of the model decreases slightly during the descending phase of the solar cycle. Our future work involves identifying days where the difference between the model and data is greatest, and days where there are more rapid variations in  $\Delta f$ , which may suggest other perturbations in the electron density.

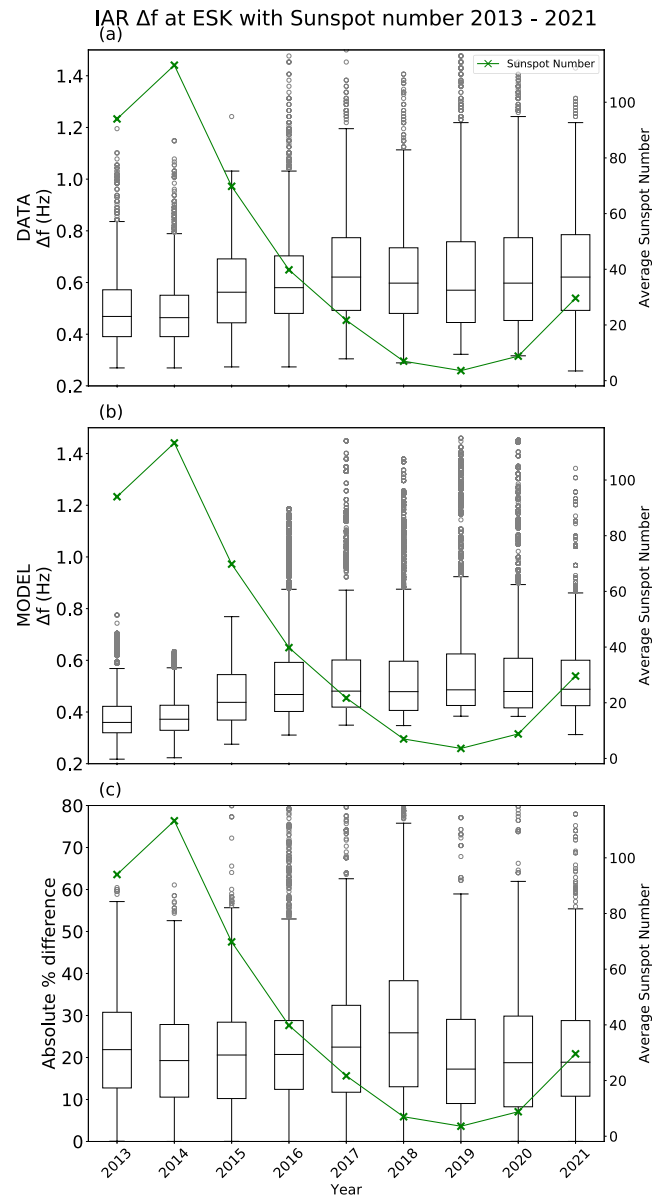


**Figure 10.** Boxplots of IAR  $\Delta f$  data (a), reduced model (b) and absolute percentage difference between the data and modeled  $\Delta f$  (c), for each year from 2013 to 2021. The right hand y axis shows the average yearly sunspot number for these years, plotted by the green line, with each year marked with a green x. Panels (a) and (b) have a y-limit of 1.5 Hz. Panel (c) has a y-limit of 80%.

### Data Availability Statement

Eskdalemuir induction coil magnetometer data was retrieved from the British Geological Survey data repository, for years 2013–2021 (British Geological Survey, 2022). Data and sample code are available here (search for induction coil): <https://webapps.bgs.ac.uk/services/ngdc/accessions/index.html>. The U-net code which detects IAR harmonics was developed by Marangio et al. (2020), and the code is available here: [github.com/marangio/unet](https://github.com/marangio/unet). We used International Reference Ionosphere (IRI) version 2016 (Bilitza et al., 2017). We used International Geomagnetic Reference Field (IGRF) version 13 (Alken et al., 2021). E-CHAIM is supported under Defence Research and Development Canada contract number W7714-186507/001/SS and is maintained by the Canadian High Arctic Ionospheric Network (CHAIN) with operations support from the Canadian Space Agency (Themens et al., 2017). The E-CHAIM website is: [chain-new.chain-project.net/index.php/projects/chain/e-chain](https://chain-new.chain-project.net/index.php/projects/chain/e-chain). Chilton Ionosonde data was used for  $f_oF_2$  measurements (RAL Space, UKSSDC, 2022). We acknowledge use of NASA/

GSFC's Space Physics Data Facility's ftp service, and OMNI data, from which we retrieved SYM-H data. The OMNI website is: [omniweb.gsfc.nasa.gov/](https://omniweb.gsfc.nasa.gov/). The Kp index data (Matzka et al., 2021) were obtained from the GFZ German Research Centre for Geosciences. The website is: [www.gfz-potsdam.de/en/section/geomagnetism/data-products-services/geomagnetic-kp-index](https://www.gfz-potsdam.de/en/section/geomagnetism/data-products-services/geomagnetic-kp-index). Sunspot numbers were obtained from the SILSO world data centre (WDC-SILSO, 2022). The data set is available here: [www.sidc.be/silso/datafiles](https://www.sidc.be/silso/datafiles).

#### Acknowledgments

R. M. Hodnett is supported by the Central England NERC Training Alliance and is a British Geological Survey BUFI student (S450). TKY acknowledges support from STFC UKRI grant ST/W00089X/1. TKY and DMW acknowledge support from NERC UKRI Grant NE/V000748/1. This research used the SPECTRE High-Performance Computing Facility at the University of Leicester. We thank the two anonymous reviewers for their constructive comments which helped to improve the manuscript.

#### References

- Alken, P., Thébaud, E., Beggan, C. D., Amit, H., Aubert, J., Baerenzung, J., et al. (2021). International geomagnetic reference field: The thirteenth generation. *Earth Planets and Space*, 73(1), 49. <https://doi.org/10.1186/s40623-020-01288-x>
- Beggan, C. D. (2014). Automatic detection of ionospheric Alfvén resonances using signal and image processing techniques. *Annales Geophysicae*, 32(8), 951–958. <https://doi.org/10.5194/angeo-32-951-2014>
- Beggan, C. D., & Musur, M. (2018). Observation of ionospheric Alfvén resonances at 1–30 Hz and their superposition with the Schumann resonances. *Journal of Geophysical Research: Space Physics*, 123(5), 4202–4214. <https://doi.org/10.1029/2018ja025264>
- Belyaev, P. P., Böisinger, T., Isaev, S. V., & Kangas, J. (1999). First evidence at high latitudes for the ionospheric Alfvén resonator. *Journal of Geophysical Research*, 104(A3), 4305–4317. <https://doi.org/10.1029/1998ja900062>
- Belyaev, P. P., Polyakov, C. V., Rapoport, V. O., & Trakhtengerts, V. Y. (1989). Experimental studies of the spectral resonance structure of the atmospheric electromagnetic noise background within the range of short-period geomagnetic pulsations. *Radiophysics and Quantum Electronics*, 32(6), 491–501. <https://doi.org/10.1007/bf01058169>
- Bilitza, D., Altadill, D., Truhlik, V., Shubin, V., Galkin, I., Reinisch, B., & Huang, X. (2017). International reference ionosphere 2016: From ionospheric climate to real-time weather predictions. *Space Weather*, 15(2), 418–429. <https://doi.org/10.1002/2016sw001593>
- Böisinger, T. (2002). Spectral properties of the ionospheric Alfvén resonator observed at a low-latitude station ( $I=1.3$ ). *Journal of Geophysical Research*, 107(A10), 1281. <https://doi.org/10.1029/2001ja005076>
- British Geological Survey. (2022). BGS induction coil magnetometer data [dataset]. BGS. (Data and sample code available to view, search for 'induction coil'.) Retrieved from <https://webapps.bgs.ac.uk/services/ngdc/accessions/index.html>
- British Geological Survey Geomagnetism. (2022). Eskdalemuir magnetic observatory. Retrieved from <https://geomag.bgs.ac.uk/operations/eskdale.html>
- Füllekrug, M., Fraser-Smith, A. C., & Reising, S. C. (1998). Ultra-slow tails of sprite-associated lightning flashes. *Geophysical Research Letters*, 25(18), 3497–3500. <https://doi.org/10.1029/98gl02590>
- Hebden, S. R., Robinson, T. R., Wright, D. M., Yeoman, T., Raita, T., & Böisinger, T. (2005). A quantitative analysis of the diurnal evolution of ionospheric Alfvén resonator magnetic resonance features and calculation of changing IAR parameters. *Annales Geophysicae*, 23(5), 1711–1721. <https://doi.org/10.5194/angeo-23-1711-2005>
- Jayalekshmi, G. L., Pant, T. K., & Prince, P. R. (2022). Sunspot-cycle evolution of major periodicities of solar activity. *Solar Physics*, 297(7), 85. <https://doi.org/10.1007/s11207-022-02017-1>
- King, J. H. (2005). Solar wind spatial scales in and comparisons of hourly wind and ace plasma and magnetic field data. *Journal of Geophysical Research*, 110(A2), A02104. <https://doi.org/10.1029/2004ja010649>
- Lysak, R. L. (1991). Feedback instability of the ionospheric resonant cavity. *Journal of Geophysical Research*, 96(A2), 1553–1568. <https://doi.org/10.1029/90ja02154>
- Lysak, R. L. (1993). Generalized model of the ionospheric Alfvén resonator. *Auroral Plasma Dynamics, Geophysical Monograph Series.*, 80(13), 121–128. <https://doi.org/10.1029/GM080p0121>
- Marangio, P., Christodoulou, V., Filgueira, R., Rogers, H. F., & Beggan, C. D. (2020). Automatic detection of ionospheric Alfvén resonances in magnetic spectrograms using U-Net. *Computers & Geosciences*, 145, 104598. <https://doi.org/10.1016/j.cageo.2020.104598>
- Matzka, J., Stolle, C., Yamazaki, Y., Bronkalla, O., & Morschhauser, A. (2021). The geomagnetic Kp index and derived indices of geomagnetic activity. *Space Weather*, 19(5), e2020SW002641. <https://doi.org/10.1029/2020sw002641>
- Molchanov, O., Schekotov, A., Fedorov, E., & Hayakawa, M. (2004). Ionospheric Alfvén resonance at middle latitudes: Results of observations at Kamchatka. *Physics and Chemistry of the Earth, Parts A/B/C*, 29(4–9), 649–655. <https://doi.org/10.1016/j.pce.2003.09.022>
- NOAA. (2022). NOAA space weather scales. Retrieved from <https://www.swpc.noaa.gov/noaa-scales-explanation>
- Nosé, M., Uyeshima, M., Kawai, J., & Hase, H. (2017). Ionospheric Alfvén resonator observed at low-latitude ground station, Muroto. *Journal of Geophysical Research: Space Physics*, 122(7), 7240–7255. <https://doi.org/10.1002/2017ja024204>
- Odzimek, A., Kulak, A., Michalec, A., & Kubisz, J. (2006). An automatic method to determine the frequency scale of the ionospheric Alfvén resonator using data from Hylaty station, Poland. *Annales Geophysicae*, 24(8), 2151–2158. <https://doi.org/10.5194/angeo-24-2151-2006>
- Parent, A., Mann, I. R., & Rae, I. J. (2010). Effects of substorm dynamics on magnetic signatures of the ionospheric Alfvén resonator. *Journal of Geophysical Research*, 115(A2), A02312. <https://doi.org/10.1029/2009JA014673>
- Polyakov, S. (1976). On properties of an ionospheric Alfvén resonator. *KAPG on Solar–Terrestrial Physics* (Vol. 3, pp. 72–73). Nauka.
- Polyakov, S., & Rapoport, V. O. (1981). The ionospheric Alfvén resonator. *Geomagnetism and Aeronomy*, 21, 610–614.
- Potapov, A. S., Polyushkina, T., Dovbnya, B., Tsegmed, B., & Rakhmatulin, R. (2014). Emissions of ionospheric Alfvén resonator and ionospheric conditions. *Journal of Atmospheric and Solar–Terrestrial Physics*, 119, 91–101. <https://doi.org/10.1016/j.jastp.2014.07.001>
- Potapov, A. S., Guglielmi, A. V., & Klain, B. I. (2022). Ratio between discrete IAR frequencies from observations in the solar cycle 24. *IEEE Transactions on Geoscience and Remote Sensing*, 60, 1–5. <https://doi.org/10.1109/tgrs.2022.3170473>
- RAL Space, UKSSDC. (2022). Chilton ionosonde data. Retrieved from [https://www.ukssdc.ac.uk/ionosondes/view\\_latest.html](https://www.ukssdc.ac.uk/ionosondes/view_latest.html)
- Ronneberger, O., Fischer, P., & Brox, T. (2015). U-Net: Convolutional networks for biomedical image segmentation. *Lecture Notes in Computer Science*, 234–241. [https://doi.org/10.1007/978-3-319-24574-4\\_28](https://doi.org/10.1007/978-3-319-24574-4_28)
- Schumann, W. O. (1952). Über die strahlungslosen eigenschwingungen einer leitenden kugel, die von einer luftschicht und einer ionosphärenhülle umgeben ist. *Zeitschrift für Naturforschung A*, 7(2), 149–154. <https://doi.org/10.1515/zna-1952-0202>
- SILSO World Data Center. (2013–2021). The international sunspot number. International sunspot number monthly bulletin and online catalogue.
- Themens, D. R., Jayachandran, P., McCaffrey, A. M., Reid, B., & Varney, R. H. (2019). A bottomside parameterization for the empirical Canadian high Arctic ionospheric model (E-CHAIM). *Radio Science*, 54(5), 397–414. <https://doi.org/10.1029/2018rs006748>

- Themens, D. R., Jayachandran, P. T., Bilitza, D., Erickson, P. J., Häggström, I., Lyashenko, M. V., et al. (2018). Topside electron density representations for middle and high latitudes: A topside parameterization for E-CHAIM based on the NeQuick. *Journal of Geophysical Research: Space Physics*, *123*(2), 1603–1617. <https://doi.org/10.1002/2017ja024817>
- Themens, D. R., Jayachandran, P. T., Galkin, I., & Hall, C. (2017). The empirical Canadian high arctic ionospheric model (E-CHAIM): NmF2 and hmF2. *Journal of Geophysical Research: Space Physics*, *122*(8), 9015–9031. <https://doi.org/10.1002/2017JA024398>
- Tsurutani, B. T., Gonzalez, W. D., Gonzalez, A. L. C., Tang, F., Arballo, J. K., & Okada, M. (1995). Interplanetary origin of geomagnetic activity in the declining phase of the solar cycle. *Journal of Geophysical Research*, *100*(A11), 21717–21733. <https://doi.org/10.1029/95JA01476>
- WDC-SILSO. (2022). Sunspot index and long term solar observations. Retrieved from [www.sidc.be/silso/datafiles](http://www.sidc.be/silso/datafiles)
- Yahnin, A. G., Semenova, N. V., Ostapenko, A. A., Kangas, J., Manninen, J., & Turunen, T. (2003). Morphology of the spectral resonance structure of the electromagnetic background noise in the range of 0.1–4 Hz at L = 5.2. *Annales Geophysicae*, *21*(3), 779–786. <https://doi.org/10.5194/angeo-21-779-2003>
- Yue, X., Wang, W., Lei, J., Burns, A., Zhang, Y., Wan, W., et al. (2016). Long-lasting negative ionospheric storm effects in low and middle latitudes during the recovery phase of the 17 March 2013 geomagnetic storm. *Journal of Geophysical Research: Space Physics*, *121*(9), 9234–9249. <https://doi.org/10.1002/2016JA022984>
- Zolotukhina, N., Polekh, N., Romanova, E., & Polyakova, A. (2014). Stability of the seasonal variations in diurnal and semidiurnal components of mid-latitude F2 layer parameters. *Advances in Space Research*, *54*(3), 342–354. <https://doi.org/10.1016/j.asr.2013.11.026>